



# Ecofriendly adsorption and sensitive detection of Hg (II) by biomass-derived nitrogen-doped carbon dots: process modelling using central composite design

Mohammed Abdullah Issa<sup>1,2</sup> · Hamid Zentou<sup>3</sup> · Zaid H. Jabbar<sup>4</sup> · Zurina Z. Abidin<sup>2</sup> · Haninah Harun<sup>2</sup> · Noor Amirah Abdul Halim<sup>5</sup> · Mohammed M. Alkhabet<sup>6</sup> · Musa Y. Pudza<sup>2</sup>

Received: 16 May 2022 / Accepted: 30 June 2022 / Published online: 8 July 2022  
© The Author(s), under exclusive licence to Springer-Verlag GmbH Germany, part of Springer Nature 2022

## Abstract

In this study, luminescent bio-adsorbent nitrogen-doped carbon dots (N-CDs) was produced and applied for the removal and detection of Hg (II) from aqueous media. N-CDs were synthesized from oil palm empty fruit bunch carboxymethylcellulose (CMC) and urea. According to several analytical techniques used, the obtained N-CDs display graphitic core with an average size of 4.2 nm, are enriched with active sites, stable over a wide range of pH and have great resistance to photobleaching. The N-CDs have bright blue emission with an improved quantum yield (QY) of up to 35.5%. The effect of the variables including pH, adsorbent mass, initial concentration and incubation time on the removal of Hg (II) was investigated using central composite design. The statistical results confirmed that the adsorption process could reach equilibrium within 30 min. The reduced cubic model ( $R^2 = 0.9989$ ) revealed a good correlation between the observed values and predicted data. The optimal variables were pH of 7, dose of 0.1 g, initial concentration of 100 mg/L and duration of 30 min. Under these conditions, adsorption efficiency of 84.6% was obtained. The adsorption kinetic data could be well expressed by pseudo-second-order kinetic and Langmuir isotherm models. The optimal adsorption capacity was 116.3 mg g<sup>-1</sup>. Furthermore, the adsorbent has a good selectivity towards Hg (II) with a detection limit of 0.01 μM due to the special interaction between Hg (II) and carboxyl/amino groups on the edge of N-CDs. This work provided an alternative direction for constructing low-cost adsorbents with effective sorption and sensing of Hg (II).

**Keywords** Optimization · Adsorption · Nitrogen-doped carbon dots · Mercury (II) ion · Nanoprobes · Mechanism

## Introduction

Environmental contamination by heavy metals due to rapid global industrialization has become a prominent issue. In specific, mercury ion is one of the greatest poisonous

contaminants that exist throughout the environment (Lee and Lee 2012; Naushad et al. 2016). With the character of series toxicity and bioaccumulation, mercury can enter into the food chain throughout air, soil and water. It has been reported that Hg (II) can cause many health problems

Responsible Editor: Angeles Blanco

✉ Mohammed Abdullah Issa  
mohammed.abdullah@sadiq.edu.iq

<sup>1</sup> Department of Oil and Gas Economics, College of Administrative and Financial Sciences, Imam Ja'afar Al-Sadiq University, Baghdad, Iraq

<sup>2</sup> Department of Chemical and Environmental Engineering, Universiti Putra Malaysia, 43400 UPM Serdang, Selangor, Malaysia

<sup>3</sup> Division of Physical Sciences and Engineering, Advanced Membranes and Porous Materials Center, King Abdullah

University of Science and Technology, Thuwal, Kingdom of Saudi Arabia

<sup>4</sup> Environmental Engineering Department, College of Engineering, University of Baghdad, Baghdad, Iraq

<sup>5</sup> Faculty of Chemical Engineering Technology, Universiti Malaysia Perlis, 02600 Arau Perlis, Malaysia

<sup>6</sup> Medical Instrumentation Technical Engineering, Al-Rasheed University College, Baghdad, Iraq

including nervous system damage, liver failure, and brain disorder. According to the Environmental Protection Agency (EPA) and World Health Organization (WHO), the maximum allowable dose of Hg (II) in drinking water is 0.01 and 0.02  $\mu\text{M}$ , respectively (Omer et al. 2019). Therefore, the separation and detection of Hg (II) from water samples is still a significant and challenging for the area of water quality.

To date, many routines have been applied for the determination of Hg (II) from aqueous media such as atomic absorption spectrophotometry, inductive-coupled plasma mass spectrometry (Jarzynska and Falandysz 2011), molecular absorption spectrophotometry (He et al. 2017), and electrochemical techniques (Kallithrakas-Kontos and Foteinis 2015). Nevertheless, these methods need sophisticated instrumentation, complex materials fabrication, time-consuming approaches, and trained personnel, which hindered their practical applications in the monitoring of Hg (II). Among these protocols, adsorption is considered the most convenient routes on basis of low-cost materials and easy operation in case that the adsorbent is accurately selected.

Over the last decades, fluorescent nanoparticles have gained extensive focusing as an adsorbent for heavy metal ions due to their high surface area, good chemical stability, and efficient adsorption capacity (Zeng et al. 2021). As one of the promising fluorescent carbon-based nanomaterials, carbon dots (CDs) have currently gathered a significant scientific attention for their spectacular characteristics such as biocompatibility, photoluminescence, and wide variety of carbon precursors used (Issa et al. 2020a). CDs typically composed of graphitic or amorphous carbon core attached to multiple functionalities with respect to production conditions and surface chemistry (Liu et al. 2017). These novel features make CDs superior in the functions of wastewater remedy, photocatalysts, COVID-19 diagnostic, and chemical detection (Meiling 2017; Li and Dong 2018; Sun and Lei 2017; Łoczechin et al. 2019; Ortega-Liebana et al. 2017; Ren et al. 2017).

Recently, different biomass-derived precursors, including cellulose have been used as lone raw materials for the synthesis of CDs (Kavitha and Kumar 2018; Hu et al. 2013; Mohapatra et al. 2015). However, the relatively weak luminescence of CDs affects higher sensitivity and thus hindered their applied functions. To solve these matters, much efforts have been employed to improve the quantum yield (QY) of CDs via doping the latter with non-metal species. In particular, N-agents drawn the interest of researchers as it can improve the PL emission via manipulating the upward shift of the Fermi level (Arul and Sethuraman 2018; Li and Dong 2018). In spite of the great physiochemical properties of nitrogen-doped CDs (N-CDs), the reported contexts still shows several drawbacks such as long duration synthesis process, weak QY and low sensitivity (Abdullah Issa et al.

2019; Dou et al. 2015; Jayaweera et al. 2019b; Liang et al. 2014; Shen et al. 2016; Wu et al. 2017b). Since the final production of N-CDs is dependent on the precursor's selection and productions conditions, it would be sensible to find a particular technique towards simplicity, low energy consumption, and more selectivity and sensitivity.

In this context, we developed N-CDs from EFB carboxymethylcellulose as a main carbon sources with the assistance of urea for short-time monitoring and removal of Hg (II) from wastewater. EFB carboxymethylcellulose are abundant with ether and hydroxyl moieties. These functional species could rise the substitution reaction resulting to the formation of CDs in rapid synthesis process. The obtained N-CDs with the optimal QY was further measured using different analytical techniques. The influence of pH, N-CDs dose, initial Hg (II) concentration, and incubation time on the adsorption of Hg (II) onto N-CDs were investigated via central composite design. The adsorption isotherms and kinetic models were further examined. Moreover, the adsorbent was employed as nanoprobe for Hg (II) detection and fruitfully applied in real water. The Hg (II) sorption and fluorescence sensing mechanism was also elaborated.

## Experimental

### Materials

CMC of oil palm empty fruit bunch (EFB) of were obtained from Waris Nove Company, Malaysia. Urea and quinine sulfate were purchased from Sigma-Aldrich (USA). Deionized water (DI) has been utilized in the entire work. All the analytical-grade chemicals were used as received without any modifications.

### Preparation of N-CDs

0.2 g of fine CMC and a rational weight of urea (depending on CCD matrix) were mixed with 25 ml of DI water. After that, the mixture was relocated to a 50 ml sealed stainless-steel reactor and heated in an oven at 270 °C for 2 h. The resulted mixture was cooled down naturally and then centrifuged at 10,000 rpm for 12 min to eliminate bulk size materials. The final solution was then placed into 0.22  $\mu\text{m}$  of vacuum filtration and 1 kDa dialysis membrane to obtain homogenous nano-sized particles.

### Characterization of adsorbent

Transmission electron microscopy (TEM) and high-resolution TEM (HRTEM) readings were analyzed via A Tecnai G2 F20 electron microscope, with an acceleration voltage of 200 kV. X-ray powder diffraction (XRD)

was carried out using PANalytical diffractometer with Cu–K $\alpha$  radiation. The Fourier transform infrared (FTIR) (Thermo Nicolet FT-IR spectrometer of 4 cm<sup>-1</sup> resolution) was performed with KBr as a standard within the range from 650 to 4000 cm<sup>-1</sup>. X-ray photoelectron spectra (XPS) (Physical Electronics PHI 5400 spectrometer, Mimos Semiconductors, Malaysia) were carried out by Al–K $\alpha$  radiation ( $h\nu = 1486.6$  eV). Prior to de-convolution, charge correction was integrated at C<sub>1s</sub> by setting binding energies of C–C and C–H at 284.8 eV. The pH values were measured via a PB-10 pH-meter (Beijing Sartorius Instruments Co. Ltd., China). UV–Vis spectra of experimental runs were measured by Shimadzu UV-1800 Spectrophotometer. Luminescence survey were recorded in quartz cuvettes with 1 cm path length using LS 55 Luminescence Spectrometer (PerkinElmer, USA) at scan rate, excitation and emission slit width of 240 nm/min, 15 nm and 5 nm, respectively.

### Batch studies

Batch adsorption tests were employed to explore the Hg (II) adsorption onto N-CDs. All tests were performed at ambient temperature by adding different mass of adsorbent selected by experimental design to flasks involving 25 ml of Hg (II) initial concentration at various pH and incubation time. A specific amount of copper nitrate was mixed with DI water to prepare 1000 ppm of stock solution. Based on standard dilution methods, different adsorbate concentrations were prepared by diluting the Hg stock solution with DI water. The experimental runs were then centrifuged at 2000 rpm and the residual Hg (II) concentration was determined from the supernatant using an atomic absorption spectrophotometer.

The equilibrium uptake  $q_e$  (mg/g) and removal efficiency (R%) were computed using the equations below:

$$q_e = \frac{(C_0 - C_e)v}{m} \quad (1)$$

$$\text{Adsorption (\%)} = \frac{C_0 - C_e}{C_0} \times 100 \quad (2)$$

where  $C_0$  and  $C_e$  (mg L<sup>-1</sup>) are the initial and equilibrium concentrations of adsorbate in solution, correspondingly,  $V$  (L) is the volume of Cu solution used, and  $m$  (g) is the weight of the adsorbent.

For isotherms studies, tests were carried out at ambient temperature using ideal pH, dosage and incubation time achieved by the RSM with varying Cu concentrations. The kinetic survey was conducted at optimal variables, in which the Hg concentration was recorded after a certain period ( $t$ ) of adsorption.

### Experimental design

In order to study the effect of the variables (pH, adsorbent dose, contact time, and initial concentration) on the removal of Hg (II), experiments were examined via RSM. Central composite design (CCD) which is utmost commonly utilized procedure of RSM was facilitated to study the optimization conditions, interaction and the main influence of the processing variables. Prior to designing the overall matrix, an initial screening experiment was conducted to select the working ranges of each factor. The input variables were set at three practical levels ( $-1, 0, +1$ ) describing the lowest, center and highest values, respectively. The experimental ranges and the levels of the independent factors for Hg (II) ion removal via N-CDs are represented in Table S1. CCD includes 2<sup>4</sup> factorial matrix with the full 27 experimental runs, involving 18 factorial points, 6 axial points, and 3 replications at the center point. The dependency of removal process to four factors were expressed via the second-order polynomial model:

$$Y = \beta_0 + \sum_{i=1}^k \beta_i x_i + \sum_{i=1}^k \beta_{ii} x_i^2 + \sum_{1 \leq i < j \leq k} \beta_{ij} x_i x_j + \varepsilon \quad (3)$$

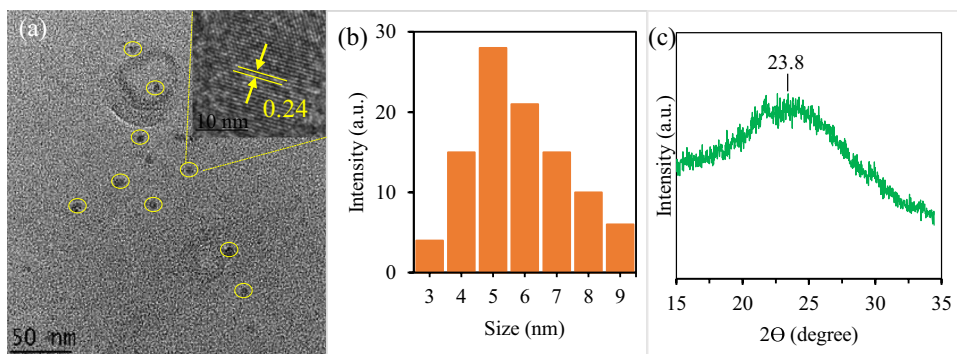
where  $Y$  represents the Hg (II) removal efficiency,  $\beta_0$  is the constant for the model,  $\beta_i$ ,  $\beta_{ii}$ , and  $\beta_{ij}$  indicate the coefficient of the linear, quadratic and interaction effect, respectively,  $x_i$  and  $x_j$  express the coded value of factors, and  $\varepsilon$  is the residual related to the runs. To assess the importance of each variable, their interaction and accuracy of the constructed model, the analysis of variance (ANOVA),  $F$ -test, and coefficient determination ( $R^2$ ) was statistically established. The design of Experts software 10.0 was employed to assess the outcome and experimental data. The CCD experimental matrix of the actual obtained response is shown in Table S2. Further elaboration on the statistical analysis was explained in our previous published works (Issa et al. 2020b).

## Results and discussion

### Physical properties of N-CDs

The TEM image in Fig. 1a indicates that the obtained N-CDs are spherical with good dispersion and uniform in size. The HRTEM image (inset of Fig. 1a) reveals that N-CDs had lattice fringes of 0.24 nm, attributing to the the (102) facet of graphite, suggesting the formation of the crystalline core. The dynamic light scattering (DLS) histogram (Fig. 1b) exhibit a narrow size distribution with an average diameter of  $4.2 \pm 0.2$  nm. Based on XRD analysis, these nanodots shows a diffraction peak at  $2\theta$  of  $23.8^\circ$  assigned to the (002) lattice spacing of graphitic-like carbon, in line with elsewhere studies (Rosa et al. 2018; Wang et al. 2017a; Wu et al. 2017a; Zhou et al. 2017).

**Fig. 1** **a** TEM image of N-CDs (inset HRTEM image), **b** particle size distribution, **c** XRD patterns



## Chemical properties of N-CDs

The XPS was employed to study the chemical edge structure of N-CDs. The XPS spectrum of CMC reveals the presence of C1s and O1s (Fig. 2a). Meanwhile, N-CDs displayed C1s, N1s and O1s, indicating that these graphitic nanodots are abundance with N. It is worth mentioning that the intensity of the as-formed N-CDs was apparently higher than that of CMC, suggesting the good surface oxidation degree. The high-resolution XPS

survey of C1s (Fig. 2b) resolved C–C, C–N, C–O, and C=O at 284.6, 285.5, 287.4, and 287.9 eV, respectively. The highest peak of  $sp^2$  conjugated C–C (52.4%) implies the effective graphitization domain (Issa et al. 2019). The  $N_{1s}$  band (Fig. 2c) displays multiple peaks at 398.8, 399.7, and 400.8 eV ascribed to graphitic N, pyridinic N and N–H respectively, infers the fruitful N-doping of CDs. Two peaks at 530.7 and 531.9 eV attributing to O–H and C=O, respectively were presented in the  $O_{1s}$  spectrum (Fig. 2d).

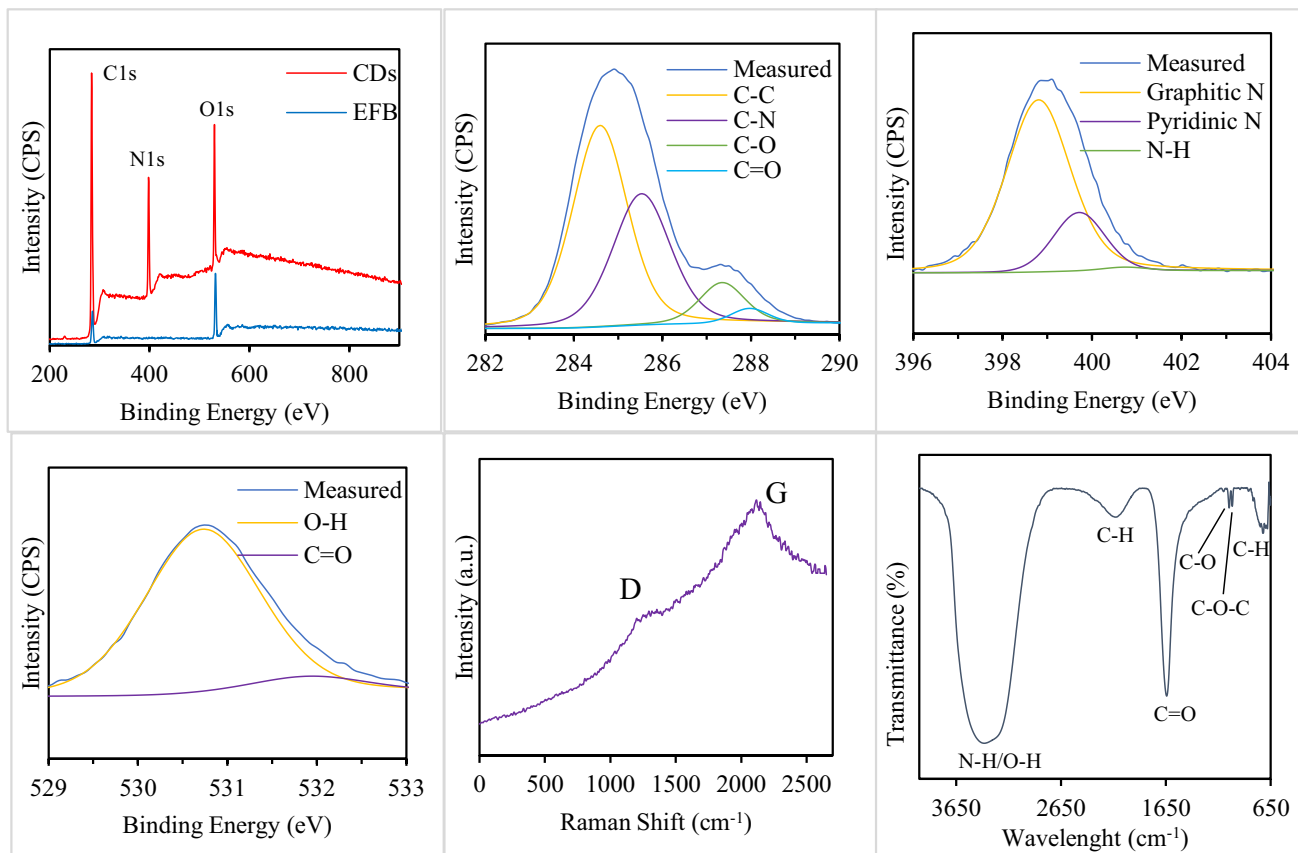


**Fig. 2** **a** XPS survey of CMC and N-CDs, high resolution, **b** C1s, **c** N1s, **d** O1s, **e** Raman spectra, **f** FTIR of N-CDs

The equivalent elemental structures are outlined Table S3. The atomic ratio of C, N and O is 67, 12, and 21, respectively, emphasizing the fruitful coating of N-molecule into the hybridized carbon domain of CDs. These atoms can manipulate the electronic nature, edge chemical properties, and PL intensity, which are essential for the selective and sensitive detection and removal of cationic ions from wastewater (Issa and Abidin 2020).

The Raman spectrum (Fig. 2e) presented multiple vibrational peaks at 1295 and 1640  $\text{cm}^{-1}$ , and these were assigned to the disordered (D) at the edge and graphitic (G) sheets of  $\text{sp}^2$  C molecules, respectively. The lower intensity peak for D band confirms the high crystallinity and graphitization index of the synthesized N-CDs (Jlassi et al. 2020). This can be clearly observed in the higher intensity of G band in contrast to that of D band. To compare the structural order between crystalline and amorphous network, the intensity ratio of  $I_G/I_D$  is typically used (Online et al. 2014). In this work, the ratio of  $I_G/I_D$  is determined to be 1.1, implying the construction of N-CDs with excellent graphitization index and graphitic-like stacking frameworks, in line with the observations of HRTEM, XRD and XPS (Huang et al. 2014).

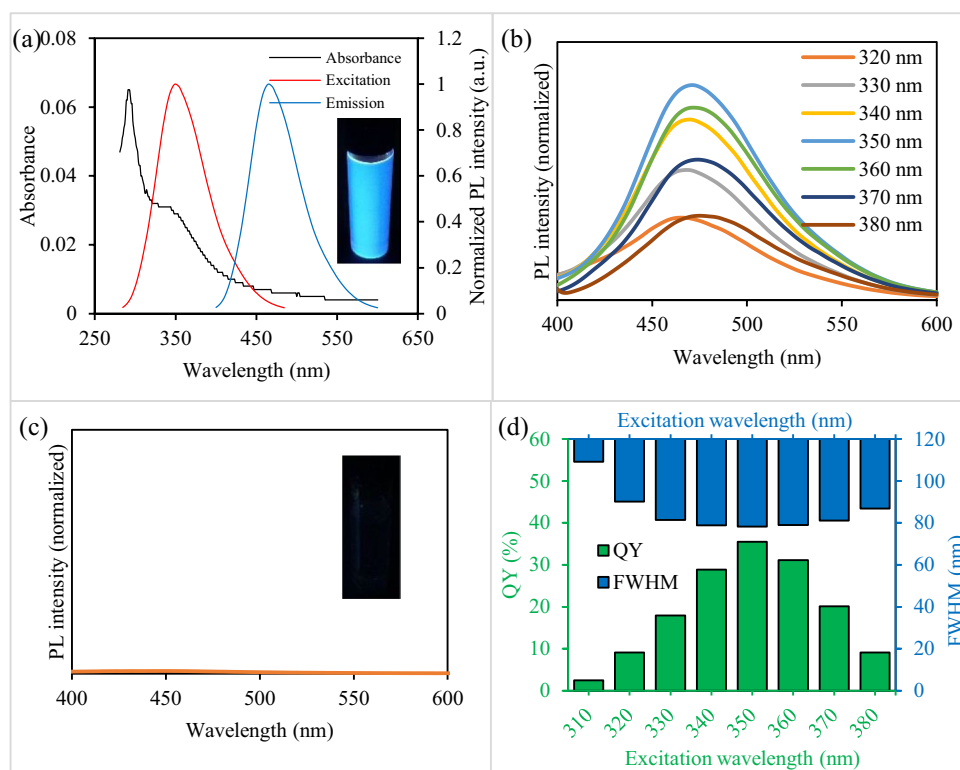
Further support about the surface functionalities was conducted via FTIR. As presented in Fig. 2f, absorption peak at 3381  $\text{cm}^{-1}$  is assigned to stretching vibration of N–H/O–H. Meanwhile, peaks placed at 2125  $\text{cm}^{-1}$  and 725  $\text{cm}^{-1}$  assigned to C–H stretching and bending vibrations, respectively (Sachdev and Gopinath 2015; Liu et al. 2016; Wu

et al. 2017b). The stretching vibration at 1641  $\text{cm}^{-1}$  is related to C=O, infers the existence of COOH moieties (Wang et al. 2017a). Moreover, the bending vibration of C–O and C–O–C appeared at 1046 and 1017  $\text{cm}^{-1}$ , respectively, verifying the formation of carbon-based oxidized species (Ortega-Liebana et al. 2017; Wang et al. 2017a). Furthermore, the presence of N–H species confirmed the successful co-doped of urea into the final domains of N-CDs as a result of sequential dehydration and passivation reactions (Rosa et al. 2018; Sachdev et al. 2014). This proves the fabrication of CDs incorporated with N, in line with data obtained from XPS.

### Optical properties of N-CDs

Optical characteristics of the CDs were studied via absorption and PL emission spectra. As displayed in Fig. 3a, the UV–Vis spectrum of the prepared N-CDs exhibits two absorption peaks centered at 294 and 350 nm. These characteristics was possibly ascribed to the  $\pi \rightarrow \pi^*$  and  $n \rightarrow \pi^*$  shift of C=C and C–O, respectively. The aqueous solution showed bright blue colour while irradiated under 365 nm UV-lamp (Fig. 3a). The PL spectra of N-CDs in Fig. 3a shows that the emission maxima at 470 nm could be observed with the maximum excitation wavelength of 350 nm. An excellent stokes-shift of 120 nm was obtained, making them superior in bioimaging functions (Ren et al. 2017). The PL excitation peak is similar to the peak depicted in UV–Vis

**Fig. 3** **a** Absorption and PL spectra of N-CDs, **b** PL spectra of N-CDs as a function of excitation wavelengths (320–380 nm), **c** PL spectra of urea, and **d** FWHM and QY versus excitation wavelength. The inset in **a** for the corresponding image under 365 nm UV light



spectra, indicating that the surface state is key factor for both absorption and PL in the N-CDs (Liu et al. 2014; Rao et al. 2018). The PL spectra in Fig. 3b displayed an excitation-dependence behaviour in which the emission was slow red-shifted as the excitation wavelength increases from 320 to 380 nm. This could be due to the size effect, surface state and molecular state, consistent with the TEM results and agrees well with the previous reports in the literature (Liu et al. 2014; Rao et al. 2018; Zhang et al. 2019). The PL spectra of urea at an excitation wavelength of 350 nm is depicted in Fig. 3c. No emission peak was noticed after the hydrothermal treatment of urea. Inset of Fig. 3c shows that urea does not fluoresce under UV excitation source, suggesting that urea mainly acts as doping agent to produce CDs from the CMC.

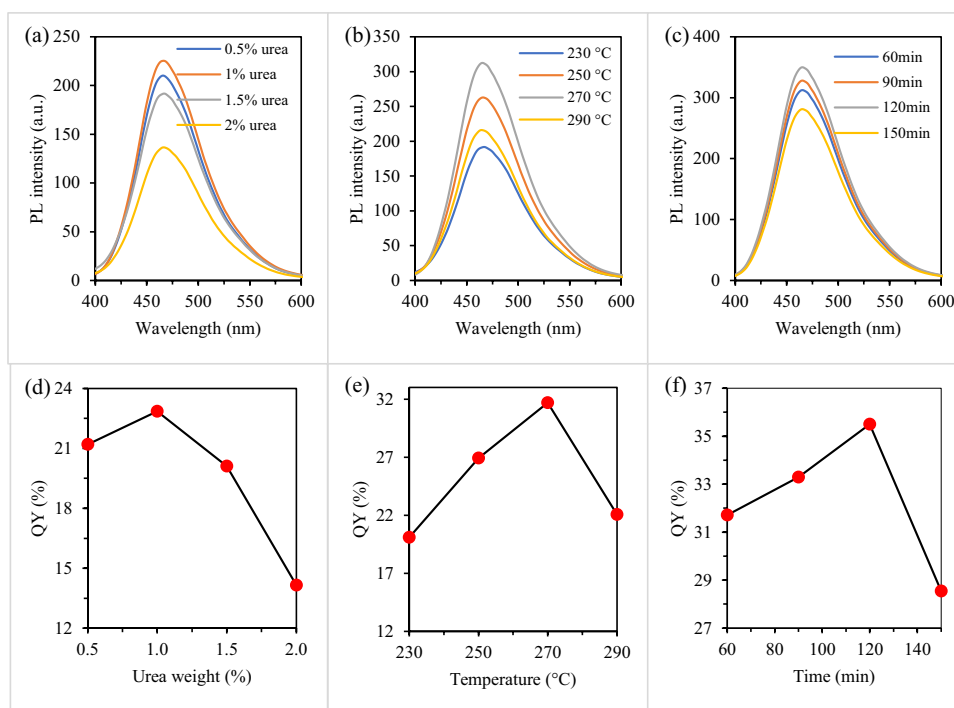
The PL spectra in terms of quantum yield (QY) and full width at half maximum (FWHM) versus excitation wavelength is displayed in Fig. 3d. The QY increases as the excitation shifted to longer wavelength, reaching the optimal percent of 35.5% at  $\lambda_{\text{ex}} = 350$  nm. Meanwhile, negative effect on the QY was noticed with increasing excitation wavelength. In addition, a minimum FWHM of 78 nm was noticed when excited at 350 nm, in which further increase or decrease in the excitation wavelength increases the FWHM value. It is worth mentioning that the lower FWHM value obtained, the more suitable of CDs to be used in a variety of functions (Wang et al. 2017b). Based on the above results, there is an obvious trade-off between QY and FWHM.

## Optimization of synthesis conditions

Since the QY is highly influenced by amino weight, temperature, and time, optimizing all these process conditions to develop N-CDs with best photophysical characteristics is necessary. Firstly, the weight of urea was varied and recorded by PL spectra (Fig. 4a, d) while the values of other parameters were kept constant at 240 °C; 1 h and 350 nm for temperature, time and absorbance wavelength, respectively. As shown in Fig. 4a, when the mass of urea varied from 0.5 to 2%, the PL emission first rises and then declines, reaching an optimal at 1%. Figure 4d reveals that maximum weight of urea was 1%, displaying a QY of 22.85%. The QY of the N-CDs was sharply declined when the urea weight was higher than 1%. Urea can interact with epoxy and carboxyl moieties to create amides and alcohols. The presence of latter lead to a multiple emissive trap between  $\pi-\pi^*$  of carbon core and thus enhance the luminescence of N-CDs. However, excessive dose of these moieties may oxidize the  $sp^2$  domains, increasing the non-radiative recombination centers and lower the QY (Rao et al. 2018; Shen et al. 2016).

The influence of reaction temperature ranging from 230 to 290 °C was investigated as depicted in Fig. 4b, e. The urea weight, time, and absorbance wavelength were kept at 1%, 1 h and 350 nm, respectively. At a temperature ranging from 230 to 270 °C, gradually rises and then declines of PL emission was observed, reaching a maximum at 270 °C. As presented in Fig. 4e, the QY

**Fig. 4** PL emission spectra and QY of N-CDs as a function of (a, d) urea weight (b, e) temperature, and (c, f) time ( $\lambda_{\text{ex}} = 350$  nm,  $\lambda_{\text{em}} = 466$  nm)



rises first to an optimal value of 31.7% at a temperature of 270 °C, followed by a reduction at higher temperature. This could be due to amino atoms penetration into the  $sp^2$  core, followed by disorders the hexagonal ring framework and forming emissive trap states leading to QY enhancement. However, excessive temperature could result in the decomposition of organic containing moieties on N-CDs edge.

The influence of time on the PL emission of N-CDs were further explored at an optimal urea weight (1%) and temperature (270 °C). As shown in Fig. 4c, the best reaction time was achieved at 120 min, in which extra rise or decline result to apparently PL loss. At an optimal reaction of 120 min, QY of 35.5% could be obtained (Fig. 4f). Therefore, based on the above data, the best processing variables for N-CDs having the optimal QY of 35.5% were 1% of urea mass, 270 °C, 120 min, shown to be more effective for producing greater QY of N-CDs in contrast to carbon dots obtained by hydrothermal route of diverse lignocellulosic wastes (Table 1).

## Photostability of N-CDs

The robustness of the fluorescent probe was studied by measuring the stability of the probe under harsh conditions, including extreme pH, high physical strength, thermostability, and long exposure time. Figure 5a shows that the PL emission is stable from pH 3 to 11. This infers the stability of the probe under a wide range of pH, which is applicable for most of metal ion sensing. Beyond 11, the emission declines due to the formation of anions as a consequence of surface chemical changes (Gao et al. 2016; Wu et al. 2017b; Yang et al. 2014). The N-CDs showed no significant loss in PL emission under high high-salt conditions (1 M NaCl) (Fig. 5a). The influence of heating on the PL intensity is presented in Fig. 5b. The N-CDs exhibited only 5% reduction in PL emission after 45 °C. However, PL declined to almost 11% with rising temperature up to 65 °C. This could be due to precipitation of the N-CDs at higher temperatures (Omer et al. 2019). For illumination time, UV-lamp excited at 365 nm was used, as presented in Fig. 5b. No apparent

**Table 1** A comparison of various cellulose-based CDs doped with heteroatom for production of CDs via hydrothermal method

Type	Raw precursors	Synthetic route	QY	Ref
CDs	CMC	210 °C, 12 h	6.2%	(Jayaweera et al. 2019a)
N-CDs	Cellulose, urea	180 °C, 72 h	21%	(Shen et al. 2016)
N-CDs	CMC, urea	210 °C, 12 h	18%	(Wu et al. 2015)
N-CDs	CMC, EDA	270 °C, 6 h	22.9%	(Abdullah Issa et al. 2019)
N-CDs	Microcrystalline cellulose, EDA	240 °C, 12 h	51%	(Wu et al. 2017b)
N/Al-CDs	Durian shell cellulose, urea, $Al(NO_3)_3$	210 °C, 12 h	28.7%	(Jayaweera et al. 2019b)
N-CDs	Durian shell cellulose, urea	210 °C, 12 h	10.4%	(Jayaweera et al. 2019b)
S-CQDs	Cellulose, sulfuric acid	200 °C, 4 h	32%	(Yang et al. 2016)
N-CDs	CMC, urea	270 °C, 2 h	35.5%	This work

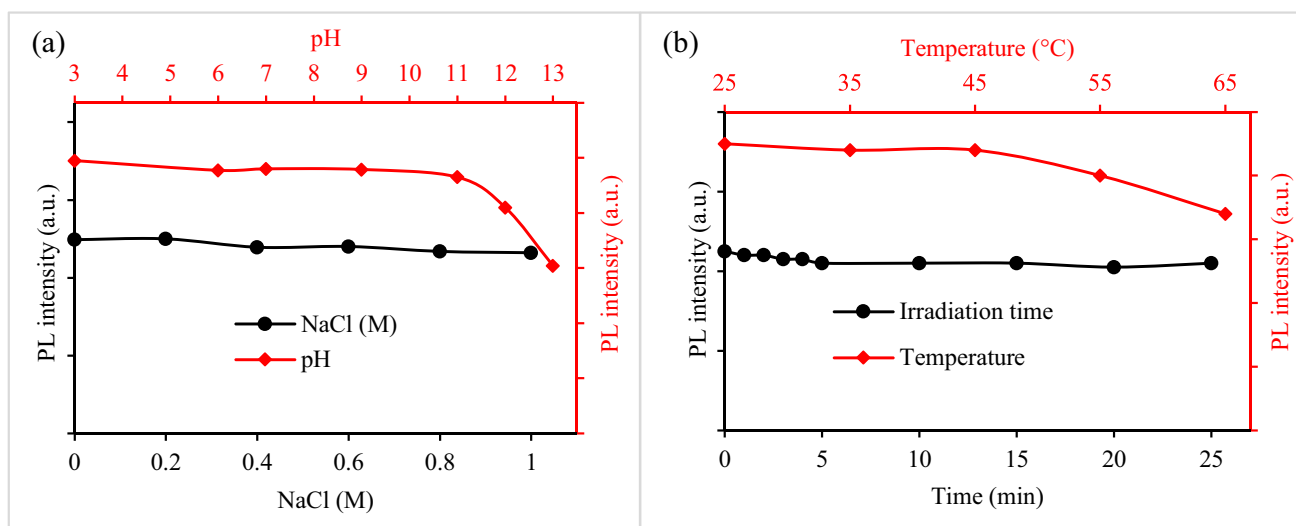


**Fig. 5** PL emission as a function of **a** pH and ionic strength and **b** temperature and illumination time

loss in PL intensity (only 3%) was observed after 25 min of exposure, implying the good resistant to photobleaching. The above observations suggest the feasibility of using these commercial nanoprobes in a variety of applications.

### Optimization of adsorption variables

Central composite design was utilized to investigate the influence of adsorption conditions including pH, adsorbent dose, initial Hg (II) concentration, and contact time on the Hg (II) removal efficiency. Based on experimental data illustrated in Table S2, the software suggested quadratic model to fit the results. However, the RSM data demonstrated that the removal ratio might be expressed by cubic model with the omit of several un necessary interactions for obtaining insignificant lack of fit and hence fitting the experimental data. According to the reduced cubic model, the dependency of the observed removal efficiency and process factors can be presented by Eq. (2)

$$\begin{aligned} \text{Removal (\%)} = & 80.88 + 5.2X_1 + 5.70X_2 + 3.70X_3 + 1.65X_4 - 2.03X_1X_2 + 0.28X_1X_3 - 1.17X_1X_4 + 1.07X_2X_3 \\ & + 0.17X_2X_4 + 1.73X_3X_4 - 10.21X_1^2 - 4.91X_2^2 + 0.091X_3^2 - 3.36X_4^2 + 1.96X_1X_2X_3 - 0.47X_1X_2X_4 + \\ & 1.09X_1X_3X_4 + 0.36X_2X_3X_4 - 5.04X_1^2X_2 + 0.32X_1^2X_3 - 0.91X_1^2X_4 + 6.29X_1X_2^2 \end{aligned} \tag{4}$$

where  $X_1$ ,  $X_2$ ,  $X_3$ , and  $X_4$  are pH, N – CDs dose, Hg (II) initial concentration and time, respectively. The positive and negative coefficient items suggest the synergetic and Antagonism effect of input factors and the predicted response, respectively.

ANOVA was performed to assess the fitness and importance of the empirical model (Table S4). The high  $F$  value (172.17) and low  $P$  value ( $<0.0001$ ) suggests that the proposed model is significant. The lack of fit (LOF) is insignificant as the  $P$  value = 0.9456, emphasizing the great model certainty (Abdullah Issa et al. 2019). The high value of determination coefficient ( $R^2 = 0.9989$ ) and the reasonable correlation between adjusted  $R^2$  (0.9931) and predicted  $R^2$  (0.9865) also proved the good fitness of constructed model for prediction of response. Moreover, coefficient of variation (CV, %), precision residual sum of square (PRESS) and adequate precision (AP) were also applied to emphasize the accuracy of the suggested model. As represented in Table S4, the CV, PRESS, and AP values were 1.57%, 59.8, and 42.14, respectively, confirm the excellent validity of the proposed model.

Figure 6a displays the correlation between experimental and model predicted values. As noticed, data distribution

forms a straight line with a standard deviation of 1.08, suggesting the robustness of the proposed model. Besides, the studentized residual against run number was analyzed (Fig. 6b). The residual plot is between reasonable range,

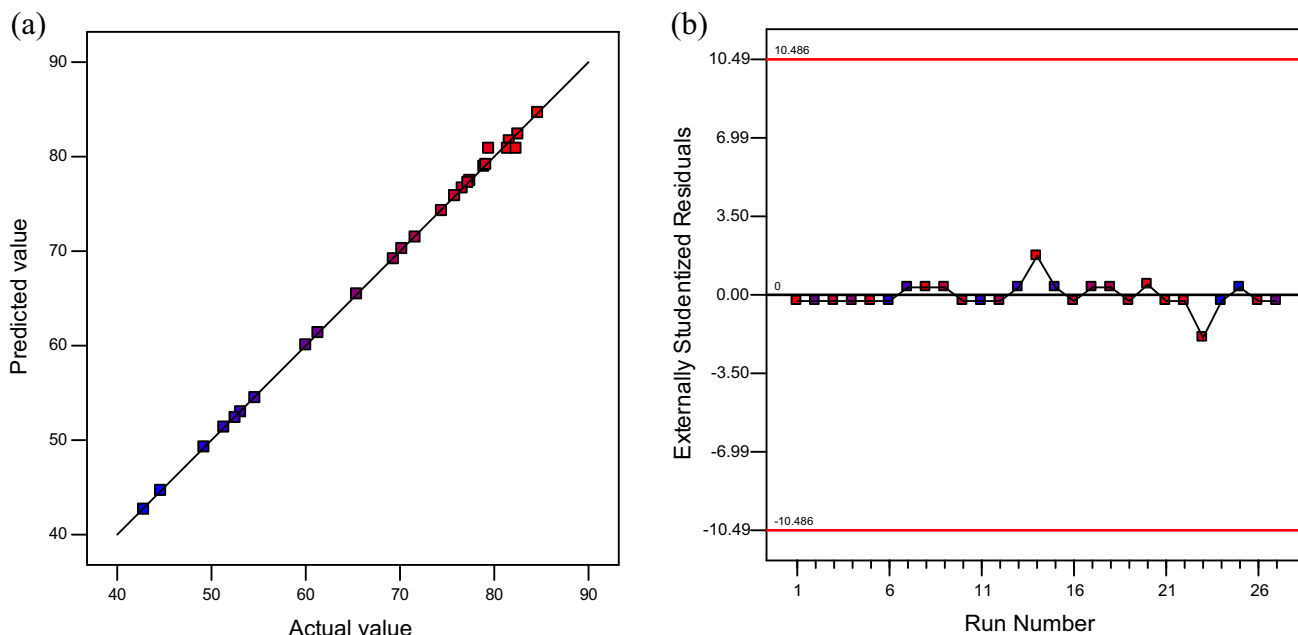
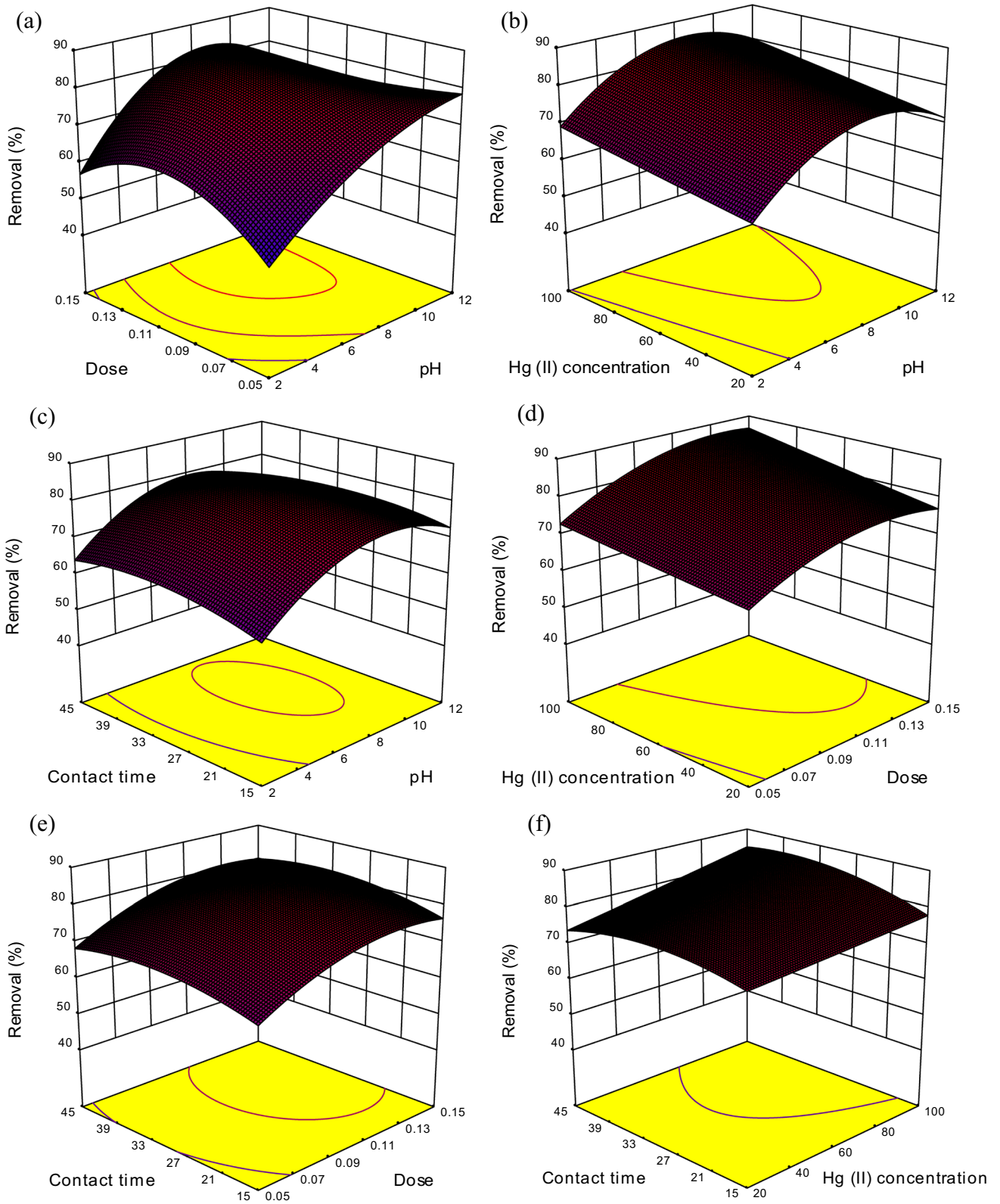


Fig. 6 a Predicted against experimental response and b externally studentized residual as a function of run number





**Fig. 7** Response surfaces plot showing the removal (%) versus the combined influence of **a**) pH-dose, **b**) pH-Hg (II) concentration, **c**) pH-time, **d**) dose-Hg (II) concentration, **e**) dose-time, **f**) time-Hg (II) concentration

justifying the fitness of the model in expressing the Hg (II) removal at various process conditions.

Figure 7 represents the influence of interaction between experimental factors on the adsorption capacity of Hg (II). In these graphs, Eq. 2 was used to facilitate plotting of 3D responses showing two varied variables within the processing range while fixing the third factor constant. Figure 7a–c illustrates the response surfaces as a function of temperature. It is obvious that the adsorption uptake rises with increasing pH and reaches the optimal when the pH is in the range of 6–9. Further increase or decrease of pH lead to an adverse effect on the Hg (II) removal efficiency. The low Hg (II) removal efficiency in acidic conditions might be due to the formation of  $H_3O^+$  ions. These ions vie Hg (II) for the functional moieties on the edge of N-CDs, making Hg (II) free in the aqueous media (Issa et al. 2020a). In natural conditions, the surface occupation reduces and Hg (II) interact with multiple active species of the adsorbent, leading to an enhancement of adsorption uptake.

The surface plots of Fig. 7a, d, and e represent the percentage adsorption for the effect of dose. As the N-CDs dose increases from 0.05 to 0.15 g, better % adsorption from 67 to 85% could be achieved. Normally, when dose increases from zero, more active groups exist, leading to the improvement of Hg (II) adsorbed. However, the higher dose up so a specific range, the less of % adsorption were obtained. This adsorption reduction might be due to the precipitation of the N-CDs particles as a consequence of reducing surface area (Issa et al. 2020a).

Figure 7b, e, and f reveals that the optimal response was determined in the initial concentration of 100 mg/L. This enhanced adsorption with increasing concentration might be attributed to the abundant driving force for mass transmission from the solution to the surface of the adsorbent. The influence of contact time in the range of 15–45 min on the response values are illustrates in Fig. 7c, e, and f. The % adsorption capacity can reach its best value within 30 min of incubation time, demonstrating the superior in terms of equilibrium time in contrast to previous reports in the literature (Ghaedi et al. 2015) (Alsuhybani et al. 2020). The above results emphasize the suitability and adequacy of the proposed system for different applications.

The contour plot of the predicted design (Figure S5) demonstrated that the optimal processing conditions values are pH (7), dose (0.1 g), initial concentration (100 mg/L) and duration (30 min). Under these conditions, a relatively high adsorption efficiency (84.6%) were obtained. The consistency between the experimental and predicted response ( $\% \text{Removal}_{\text{pred}}$  84.8%) suggest the validity and suitability of proposed model for predication of adsorptive uptake of N-CDs for Hg (II) ions.

## Adsorption isotherm and kinetic model

In order to gather enriched information into the adsorbate-adsorbent interaction, Langmuir and Freundlich isotherm models were analysed. The isotherms isotherm of N-CDs for Hg (II) were investigated using the best conditions at ambient temperature. The relevant factors are summarized in Table S6. The results emphasize that Langmuir equation with  $R^2$  (0.9946) fits well the experimental data than Freundlich isotherm ( $R^2 = 0.9865$ ), implying that the adsorption process is monolayer. The maximum adsorption uptake of 116.3 mg/g was determined. A summary of different adsorbents used for Hg (II) removal (Table S7) suggest the superior performance of the present work to adsorb Hg (II).

Hg (II) adsorption as a function of contact time was further explored and the results are illustrated in Table S8. The pseudo-first-order and second-order kinetics are important in wastewater treatment as it observe the adsorbent-adsorbate dynamic process. As presented in Fig. 8d, e, the pseudo second-order equation with  $R^2 = 0.9787$  is greater than that of the first-order equation ( $R^2 = 0.9986$ ), suggesting that the chemisorption is responsible for the sorption behavior onto the N-CDs.

Reusability is a significant principle for nanomaterials to be applicable in practical functions. Thus, the adsorption–desorption series were carried out using the eluent of ascorbic acid (1 mol/L). As illustrated in Figure S9, no apparent decline in the % adsorption (only 10%) after five desorption cycles. This reduction might be ascribed to the irreversible occupation of the active adsorbent sites. The above data indicate that N-CDs could be effectively reused and recycled.

## Fluorescence detection

Notably, the existence of functional moieties including hydroxyl, carboxyl and amino groups on the N-CDs surface can make a connection to interact these nanomaterials with specific ions (Patir and Gogoi 2018). In this regard, the feasibility of using N-CDs as fluorescent probes for mercury ions was applied via measuring the PL signal of the proposed N-CDs. The PL response of N-CDs was conducted by adding different Hg (II) concentrations in a range of 0–50  $\mu\text{M}$ . As presented in Fig. 9a, the PL signal decreases slowly with the rise in the Hg (II) concentration. The quenching performance was further established via Stern–Volmer equation. The turn-off factors ( $I_0/I$ ) against the concentration of Hg (II) displayed a straight-line calibration plot in the range of 0–50  $\mu\text{M}$ , with a correlation coefficient of 0.9999 (Fig. 9b). Figure 9b (inset) signifies the fluorescence emission of nanoprobe with and without adding 100  $\mu\text{M}$  Hg (II) ions under 365 nm UV-excitation light.

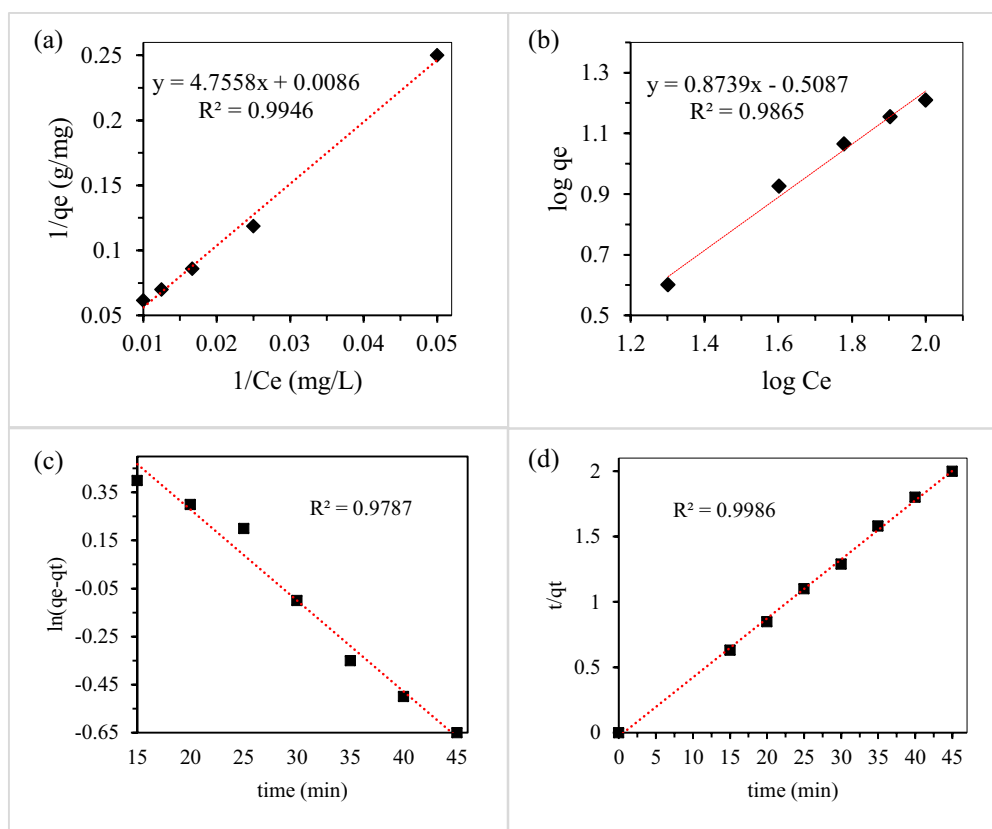


**Fig. 8** Adsorption isotherms with two models: **a** Langmuir model. **b** Freundlich model

The obvious turn-off in the blue emission is consistent with the data emphasized by PL spectra. The turn-off behavior of the Hg (II) on N-CDs could be expressed as  $(I_0 - I)/I_0 = 0.9155 + 0.0181 [C]$ , where  $I$  and  $I_0$  is the PL emission at 470 nm in the presence and absence of Hg (II), respectively and  $[C]$  is the Hg (II) concentration. The limit of detection (LOD) was estimated by  $3\sigma/K$  and found to be 0.01  $\mu\text{M}$ . Table S10 summarizes the comparison between the constructed nanoprobe with other previously reported CD-based Hg (II) sensors. Obviously, the proposed sensing system is comparable to other methods in terms of lower detection limit and wider linear ranges.

The analytical determination of mercury (II) in real samples displays a challenge to the practical analysis due to their inherent pollution with other metal ions. Thus, the applicability of the sensing platform was evaluated in the sensing of Hg (II) by recording the PL signal of aqueous N-CDs with 100  $\mu\text{M}$  of Hg (II) alone and mixed with 100  $\mu\text{M}$  of several metal ions. Hg (II) can turn off the emission of N-CDs, while low to none effect of other concomitant metal ions on the PL emission was noticed (Fig. 9c). In fact, the nature of chelating species on the edge of nanoprobe plays a key role in the metal-ion selectivity and coordination kinetics. Therefore, the particular selectivity of N-CDs towards Hg (II) among

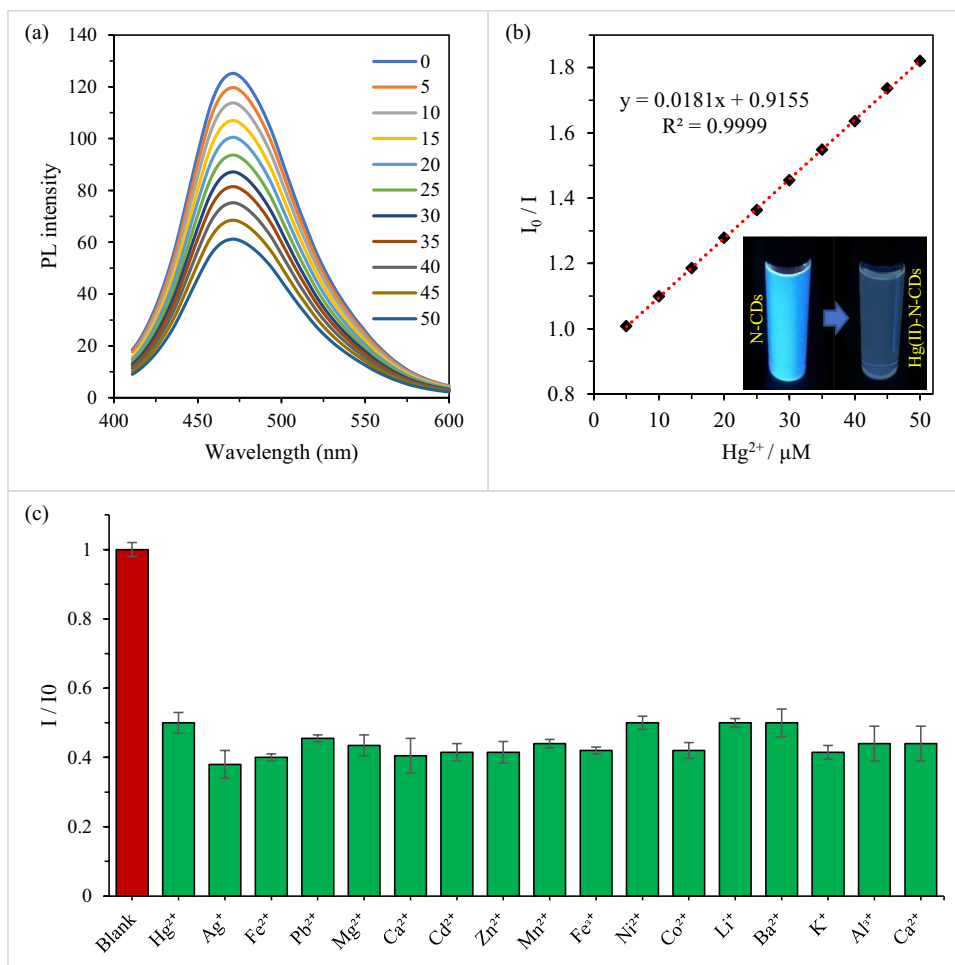
other metal ions might be assigned to the strong coordination of Hg (II) for the O, N electron donors (Issa et al. 2020b). As a result, the formation of new binding atoms might lead to the transfer of the excited energy to the d-orbital of Hg (II). The above finding indicates the anti-intrusion capability of the developed fluorescent probes for sensing Hg (II).

The applicability of the sensing platform in the monitoring of Hg (II) was further validated in tap water by spiking different concentrations of Hg (II) solution. As presented in Table S11, the recoveries were varying from 91.7 to 99.6 with the relative standard deviation (RSD %) of less than 2.6%. According to the above results, the proposed sensing nanoprobe can monitor Hg (II) quantitatively in real water samples.

### Hg (II) sorption and sensing mechanism

To get a clear insight of the sorption mechanism, the N-CDs after adsorption processes was measured via FTIR (Figure S12a). After sorption, the  $1641\text{ cm}^{-1}$  intense peak corresponded to C=O stretching vibration weakened. In addition, the  $1045$  and  $1016\text{ cm}^{-1}$  peaks related to C–O and C–O–C bending vibrations increased and red-shifted to  $955\text{ cm}^{-1}$ . Moreover, the  $725\text{ cm}^{-1}$  peak associated with C–H moieties significantly increased. Furthermore, the additional of

**Fig. 9** **a** Fluorescence spectra of N-CDs versus Hg (II) concentrations excited at 350 nm, **b** calibration graph of N-CDs with increasing the concentration of Hg (II). The inset shows the suspension with the absence and presence of Hg (II) under UV illumination source, **c** selectivity of N-CDs for coexisting other metal ions with Hg (II)



1214  $\text{cm}^{-1}$  peak indicates the binding affinity of N to Hg (II). The results of FTIR emphasize the involvement of the carboxyl and amino in the Hg (II) sorption.

TEM spectra was further analyzed to understand the Hg (II) removal by N-CDs as displayed in Figure S12b. A great increase in the size of N-CDs–Hg (II) could be seen. The distribution area is in the range of 7–15 nm with an average size of 8.6 nm. In contrast to the paired N-CDs, the size distribution increment suggests the precipitation of N-CDs leading to the N-CDs–Hg (II) nanocomplex formation. Furthermore, the dependency of PL emission on the temperature was also measured. The PL intensity of the nanocomplexes gradually declines as the temperature rises (Figure S12c). This might be assigned to the partially quenched of undissolved nanocomplexes in the suspension leading to the static turn-off behavior (Lakowicz 2006; Bandi et al. 2018). Based on the above-mentioned investigations, the N-CDs adsorbent had a good adsorption uptake. As a result, electrostatic bindings between Hg (II) and carboxylic/ amino species on the edge of N-CDs, leading to PL turn-off mechanism.

## Conclusion

The purpose of the recent paper is to construct a simple, sensitive and inexpensive route for efficient Hg (II) removal and detection in real water. The bright fluorescence N-CDs were constructed without using harsh reagents or high-energy consumption. The as-obtained N-CDs have a great graphitization index, are attached to various functional groups and have great resistance for aging conditions. By studying the effect of synthetic conditions on the optical characteristics of N-CDs, optimal QY of 35.5% was determined. The influence of parameters on Hg (II) sorption was statistically analyzed via central composite design (CCD) combined with response surface methodology (RSM). The N-CDs had great adsorption characteristics, with utmost adsorption capacity of 116.3  $\text{mg g}^{-1}$ . Moreover, the adsorbent was applied for selective and sensitive determination of Hg (II) with linear response ranges between 0 and 50  $\mu\text{M}$  and a detection limit of 0.01  $\mu\text{M}$ . According to the vast data, coordination complexes were formed as a result of binding Hg (II) to  $-\text{COOH}/-\text{NH}$  groups around N-CDs, resulting to charge transfer and

fluorescent turn-off mechanism. The N-CDs have the capability to monitor Hg (II) in real water with reasonable results. It is believed that the present approach may offer a new way for developing low-cost, highly luminescence, great Hg (II) removal and detection in environmental applications.

**Supplementary Information** The online version contains supplementary material available at <https://doi.org/10.1007/s11356-022-21844-0>.

**Acknowledgements** The first author would like to thank Imam Ja'afar Al-Sadiq University, Iraq, for their continued support and encouragement to publish in reputable journals.

**Authors' contributions** Conceptualization, methodology, experimental work, data analysis, writing—original draft, visualization, writing—review and editing were conducted by M.A.I. Z.Z.A. was contributed in data curation, resources, investigation, supervision. This was done together with H.Z., Z.H.J., H.H. N.A.A.H., M.M.A., and M.Y.P., who also contributed reagents/materials/analysis tools/ paper editing.

**Funding** This research context is supported by the UPM under the GP-IPS/2017/9556800 grant.

**Data availability** Supplementary data related to this work can be found in the archive document.

## Declarations

**Ethical approval** Not applicable.

**Consent to participate** Not applicable.

**Competing interests** The authors declare that they have no competing interests.

## References

- Abdullah Issa M, Abidin ZZ, Sobri S, Abdul-Rashid S, Mahdi MA, Ibrahim NA, Pudza MY (2019) Fabrication, characterization and response surface method optimization for quantum efficiency of fluorescent nitrogen-doped carbon dots obtained from carboxymethylcellulose of oil palms empty fruit bunch. *Chin J Chem Eng* 28(2):584–592. <https://doi.org/10.1016/j.cjche.2019.04.003>
- Alsuhybani M, Alshahrani A, Algami M, Al-Kahtani AA, Alqadami AA (2020) Highly efficient removal of Pb(II) from aqueous systems using a new nanocomposite: adsorption, isotherm, kinetic and mechanism studies. *J Mol Liq* 301:112393. <https://doi.org/10.1016/j.molliq.2019.112393>
- Arul V, Sethuraman MG (2018) Facile green synthesis of fluorescent N-doped carbon dots from *Actinidia deliciosa* and their catalytic activity and cytotoxicity applications. *Opt Mater* 78:181–190
- Bandi R, Devulapalli NP, Dadigala R, Gangapuram BR, Guttena V (2018) Facile conversion of toxic cigarette butts to N, S-codoped carbon dots and their application in fluorescent film, security ink, bioimaging, sensing and logic gate operation. *ACS Omega* 3(10):13454–13466. <https://doi.org/10.1021/acsomega.8b01743>
- Dou Q, Fang X, Jiang S, Chee PL, Lee TC, Loh XJ (2015) Multifunctional fluorescent carbon dots with antibacterial and gene delivery properties. *RSC Adv* 5(58):46817–46822
- Gao X, Du C, Zhuang Z, Chen W (2016) Carbon quantum dot-based nanoprobe for metal ion detection. *J Mater Chem C* 4(29):6927–6945
- Ghaedi AM, Ghaedi M, Vafaei A, Iravani N, Keshavarz M, Rad M, ..., Gupta VK (2015) Adsorption of copper (II) using modified activated carbon prepared from Pomegranate wood: Optimization by bee algorithm and response surface methodology. *J Mol Liq* 206:195–206. <https://doi.org/10.1016/j.molliq.2015.02.029>
- He M, Huang L, Zhao B, Chen B, Hu B (2017) Advanced functional materials in solid phase extraction for ICP-MS determination of trace elements and their species - A review. *Anal Chim Acta* 973:1–24. <https://doi.org/10.1016/j.aca.2017.03.047>
- Hu L, Sun Y, Li S, Wang X, Hu K, Wang, L, ..., Wu Y (2013) Multifunctional carbon dots with high quantum yield for imaging and gene delivery. *Carbon* 67:508–513
- Huang H, Li C, Zhu S, Wang H, Chen C, Wang Z, ..., Feng S (2014) Histidine-derived nontoxic nitrogen-doped carbon dots for sensing and bioimaging applications. *Langmuir* 30(45):13542–13548. <https://doi.org/10.1021/la503969z>
- Issa MA, Abidin ZZ (2020) Sustainable development of enhanced luminescence polymer-carbon dots composite film for rapid Cd<sup>2+</sup> removal from wastewater. *Molecules* 25(15). <https://doi.org/10.3390/molecules25153541>
- Issa MA, Abidin ZZ, Pudza MY, Zentou H (2020a) Efficient removal of Cu(II) from aqueous systems using enhanced quantum yield nitrogen-doped carbon nanodots. *RSC Adv* 10(25):14979–14990
- Issa MA, Abidin ZZ, Sobri S, Rashid SA, Mahdi MA, Ibrahim NA (2020b) Fluorescent recognition of Fe<sup>3+</sup> in acidic environment by enhanced-quantum yield N-doped carbon dots: optimization of variables using central composite design. *Sci Rep* 10(1):11710. <https://doi.org/10.1038/s41598-020-68390-8>
- Issa MA, Abidin ZZ, Sobri S, Rashid S, Mahdi MA, Ibrahim NA, Pudza MY (2019) Facile synthesis of nitrogen-doped carbon dots from lignocellulosic waste. *Nanomaterials* 9(10):1500
- Jarzynska G, Falandysz J (2011) The determination of mercury in mushrooms by CV-AAS and ICP-AES techniques. *J Environ Sci Health A Tox Hazard Subst Environ Eng* 46(6):569–573. <https://doi.org/10.1080/10934529.2011.562816>
- Jayaweera S, Yin K, Hu X, Ng WJ (2019a) Facile preparation of fluorescent carbon dots for label-free detection of Fe<sup>3+</sup>. *J Photochem Photobiol A Chem* 370(October 2018):156–163. <https://doi.org/10.1016/j.jphotochem.2018.10.052>
- Jayaweera S, Yin K, Hu X, Ng WJ (2019b) Fluorescent N/Al Co-Doped Carbon Dots from Cellulose Biomass for Sensitive Detection of Manganese (VII). *J Fluoresc* 29:1291–1300. <https://doi.org/10.1007/s10895-019-02452-7>
- Jlassi K, Eid K, Sliem MH, Abdullah AM, Chehimi MM, Krupa I (2020) Rational synthesis, characterization, and application of environmentally friendly (polymer-carbon dot) hybrid composite film for fast and efficient UV-assisted Cd<sup>2+</sup> removal from water. *Environ Sci Eur* 32(1). <https://doi.org/10.1186/s12302-020-0292-z>
- Kallithrakas-Kontos N, Foteinis S (2015) Recent advances in the analysis of mercury in water - review. *Curr Anal Chem* 12:22–36
- Kavitha T, Kumar S (2018) Turning date palm fronds into biocompatible mesoporous fluorescent carbon dots. *Sci Rep* 8(1):1–10
- Lakowicz JR (2006) Principles of fluorescence spectroscopy. In: Lakowicz JR (ed) Springer, 3rd edn. Springer, Baltimore
- Lee KJ, Lee TG (2012) A review of international trends in mercury management and available options for permanent or long-term mercury storage. *J Hazard Mater* 241–242:1–13. <https://doi.org/10.1016/j.jhazmat.2012.09.025>
- Li L, Dong T (2018) Photoluminescence tuning in carbon dots: surface passivation or/and functionalization, heteroatom doping. *J Mater Chem C* 6(30):7944–7970

- Liang Z, Zeng L, Cao X, Wang Q, Wang X, Sun R (2014) Sustainable carbon quantum dots from forestry and agricultural biomass with amplified photoluminescence by simple NH<sub>4</sub>OH passivation. *J Mater Chem C* 2(45):9760–9766
- Liu H, Zhao X, Wang F, Wang Y, Guo L, Mei J, ..., Zhao D (2017) High-efficient excitation-independent blue luminescent carbon dots. *Nanoscale Res Lett* 12:0–6
- Liu J, Liu X, Luo H, Gao Y (2014) One-step preparation of nitrogen-doped and surface-passivated carbon quantum dots with high quantum yield and excellent optical properties. *RSC Adv* 4(15):7648
- Liu Y, Zhou Q, Li J, Lei M, Yan X (2016) Selective and sensitive chemosensor for lead ions using fluorescent carbon dots prepared from chocolate by one-step hydrothermal method. *Sensors Actuators B Chem* 237:597–604
- Łoczechin A, Séron K, Barras A, Giovanelli E, Belouzard S, Chen YT, ..., Szunerits S (2019) Functional carbon quantum dots as medical countermeasures to human coronavirus. *ACS Appl Mater Interfaces* 11(46):42964–42974. <https://doi.org/10.1021/acsami.9b15032>
- Meiling TT (2017) Development of a reliable and environmentally friendly synthesis for fluorescence carbon nanodots. PhD thesis, University of Potsdam, Germany
- Mohapatra S, Sahu S, Sinha N, Bhutia SK (2015) Synthesis of a carbon-dot-based photoluminescent probe for selective and ultrasensitive detection of Hg<sup>2+</sup> in water and living cells. *Analyst* 140(4):1221–1228
- Naushad M, Ahamad T, Sharma G, Al-Muhtaseb AH, Albadarin AB, Alam MM, ..., Ghfar AA (2016) Synthesis and characterization of a new starch/SnO<sub>2</sub> nanocomposite for efficient adsorption of toxic Hg<sup>2+</sup> metal ion. *Chem Eng J* 300:306–316. <https://doi.org/10.1016/j.cej.2016.04.084>
- Omer KM, Hama Aziz KH, Mohammed SJ (2019) Improvement of selectivity: Via the surface modification of carbon nanodots towards the quantitative detection of mercury ions. *New J Chem* 43(33):12979–12986
- Online VA, Teng X, Ge C, Yan M, Yang J, Zhang Y, ..., Bi H (2014) Green synthesis of nitrogen-doped carbon dots from konjac flour with “off–on” fluorescence by Fe<sup>3+</sup> and L-lysine for bioimaging. *Mater Chem B* 20:4631–4639
- Ortega-Liebana MC, Chung NX, Limpens R, Gomez L, Hueso JL, Santamaria J, Gregorkiewicz T (2017) Uniform luminescent carbon nanodots prepared by rapid pyrolysis of organic precursors confined within nanoporous templating structures. *Carbon* 117:437–446
- Patir K, Gogoi SK (2018) Nitrogen-doped carbon dots as fluorescence ON–OFF–ON sensor for parallel detection of copper(II) and mercury(II) ions in solutions as well as in filter paper-based microfluidic device†. *Nanoscale Adv* 1(2):592–601
- Rao L, Tang Y, Lu H, Yu S, Ding X, Xu K, ..., Zhang JZ (2018) Highly photoluminescent and stable N-doped carbon dots as nanoprobe for Hg<sup>2+</sup> detection. *Nanomaterials* 8(11):1–18. <https://doi.org/10.3390/nano8110900>
- Ren G, Zhang Q, Li S, Fu S, Chai F, Wang C, Qu F (2017) One pot synthesis of highly fluorescent N doped C-dots and used as fluorescent probe detection for Hg<sup>2+</sup> and Ag<sup>+</sup> in aqueous solution. *Sensors Actuators B Chem* 243:244–253
- Rosa da SSD, Caminhas, Durães L, Mesquita D, Paulo J, Pereira Vargas F (2018) Luminescent carbon dots obtained from cellulose. *Mater Chem Phys* 203:148–155
- Sachdev A, Gopinath P (2015) Green synthesis of multifunctional carbon dots from coriander leaves and their potential application as antioxidants, sensors and bioimaging agents. *Analyst* 140(12):4260–4269
- Sachdev A, Matai I, Gopinath P (2014) Implications of surface passivation on physicochemical and bioimaging properties of carbon dots. *RSC Adv* 4(40):20915–20921
- Shen P, Gao J, Cong J, Liu Z, Li C, Yao J (2016) Synthesis of cellulose-based carbon dots for bioimaging. *ChemistrySelect* 1(7):1314–1317. <https://doi.org/10.1002/slct.201600216>
- Sun X, Lei Y (2017) Fluorescent carbon dots and their sensing applications. *TrAC Trends Anal Chem* 89:163–180
- Wang R, Wang X, Sun Y (2017a) One-step synthesis of self-doped carbon dots with highly photoluminescence as multifunctional biosensors for detection of iron ions and pH. *Sensors Actuators B Chem* 241:73–79
- Wang Y, Zhu Y, Yu S, Jiang C (2017b) Fluorescent carbon dots: rational synthesis, tunable optical properties and analytical applications. *RSC Adv* 7:40973–40989
- Wu F, Su H, Wang K, Wong WK, Zhu X (2017a) Facile synthesis of N-rich carbon quantum dots from porphyrins as efficient probes for bioimaging and biosensing in living cells. *Int J Nanomed* 12:7375–7391. <https://doi.org/10.2147/IJN.S147165>
- Wu P, Li W, Wu Q, Liu Y, Liu S (2017b) Hydrothermal synthesis of nitrogen-doped carbon quantum dots from microcrystalline cellulose for the detection of Fe<sup>3+</sup> ions in an acidic environment. *RSC Adv* 7(70):44144–44153
- Wu Q, Li W, Tan J, Wu Y, Liu S (2015) Hydrothermal carbonization of carboxymethylcellulose: One-pot preparation of conductive carbon microspheres and water-soluble fluorescent carbon nanodots. *Chem Eng J* 266:112–120. <https://doi.org/10.1016/j.cej.2014.12.089>
- Yang G, Wan X, Su Y, Zeng X, Tang J (2016) Acidophilic S-doped carbon quantum dots derived from cellulose fibers and their fluorescence sensing performance for metal ions in an extremely strong acid environment. *J Mater Chem A* 4(33):12841–12849. <https://doi.org/10.1039/c6ta05943k>
- Yang Z, Xu M, Liu Y, He F, Gao F, Su Y, ..., Zhang Y (2014) Nitrogen-doped, carbon-rich, highly photoluminescent carbon dots from ammonium citrate. *Nanoscale* 6(3):1890–1895
- Zeng H, Hu Z, Peng C, Deng L, Liu S (2021) Effective adsorption and sensitive detection of Cr(VI) by chitosan/cellulose nanocrystals grafted with carbon dots composite hydrogel. *Polymers* 13(21). <https://doi.org/10.3390/polym13213788>
- Zhang L, Liu W, Zhuang H, Zhang J, Chen C (2019) Environmentally friendly synthesis of photoluminescent biochar dots from waste soy residues for rapid monitoring of potentially toxic elements. *RSC Adv* 9:21653–21659. <https://doi.org/10.1039/c9ra03001h>
- Zhou J, Zhou H, Tang J, Deng S, Yan F, Li W, Qu M (2017) Carbon dots doped with heteroatoms for fluorescent bioimaging: a review. *Microchim Acta* 184(2):343–368

**Publisher's note** Springer Nature remains neutral with regard to jurisdictional claims in published maps and institutional affiliations.